Tectonophysics 858 (2023) 229850

Contents lists available at ScienceDirect

Tectonophysics

journal homepage: www.elsevier.com/locate/tecto

Low-temperature plastic rheology of granitic feldspar and quartz

Michael K. Sly [a,*], Katharine Padilla [b], Katharine M. Flores [c,b], Philip Skemer [a]

[a] Department of Earth and Planetary Sciences, Washington University in Saint Louis, United States of America
[b] Institute of Materials Science and Engineering, Washington University in Saint Louis, United States of America
[c] Department of Mechanical Engineering and Materials Science, Washington University in Saint Louis, United States of America

ARTICLE INFO

Keywords:
Low-temperature plasticity
Feldspar
Quartz
Nanoindentation

ABSTRACT

Deformation of the Earth's continental crust depends largely on the mechanical properties of quartz and feldspar, including deformation by brittle, semi-brittle, and elastoplastic mechanisms. However, elastoplastic deformation of these mineral phases is difficult to achieve in laboratory experiments at temperatures relevant to the upper crust without high confining pressures to suppress microcracking and macroscopic brittle failure. In this study we use instrumented nanoindentation to determine the plastic yield strength of quartz, and orthoclase and plagioclase feldspars at temperatures of 23–500 °C and at strain rates of $\sim 10^{-2}$ s^{-1}. The specimen investigated here is a medium-grained granite from southwestern Rhode Island, grains of which were characterized and oriented using scanning electron microscopy and electron backscatter diffraction (EBSD). Indentation hardness and modulus of oriented grains was measured directly using a diamond Berkovich nanoindenter; these quantities were then used to calculate yield stresses through several existing theoretical and numerical models. The calculated yield stresses are fit to constitutive flow laws for low-temperature plasticity. We find that, in contrast to most observations from nature, quartz is systematically stronger than both feldspars. The conditions of these experiments are comparable to those near the tips of cracks in the mid to upper crust and the results presented here are particularly relevant to geologic settings where brittle and semi-brittle processes dominate, including aseismic creep of faults.

1. Introduction

Within orogenic belts and plate boundary shear zones, deformation of the upper and mid-continental crust is controlled significantly by the mechanical properties of quartz and feldspar (e.g., Tullis, 2002; Tullis and Yund, 1992). At the shallowest depths deformation is entirely brittle, but with increasing temperature and pressure deformation becomes semi-brittle, and ultimately fully plastic (e.g., Sibson, 1977). Analysis of shear zones provide important constraints on the conditions where these rheological transitions occur. For example, studies of naturally deformed quartzofeldspathic rocks show that plastic deformation may occur at temperatures as low as 300 °C, and that the complete transition from brittle to fully viscous deformation occurs between ~300 and 450 °C (e.g., Fossen and Cavalcante, 2017; Papeschi et al., 2018; Stipp et al., 2002b, 2002a; Tullis, 2002). This range of conditions may also correspond to the strongest parts of the continental crust (e.g., Bürgmann and Dresen, 2008; Kohlstedt et al., 1995).

The rheology of both quartz and feldspar has been studied individually and in aggregate, including extensive experimentation at high temperatures ($T \geq 500$ °C for quartz: e.g. Gleason and Tullis, 1995; Richter et al., 2018; $T \geq 850$ °C for feldspars: e.g. Rybacki and Dresen, 2000; Xiao et al., 2002); and $T \geq 700$ °C for quartz-feldspar aggregates: e.g. Holyoke III and Tullis, 2006; Xiao et al., 2002)). By necessity, most studies that are used to investigate viscoplastic rheology are conducted at temperatures, pressures, and strain rates that are greater than the deformation conditions relevant to the upper and mid-crust (e.g., Hirth and Tullis, 1992; Rybacki and Dresen, 2004). Due to the large extrapolation in temperature and strain-rate, and likely changes in deformation mechanism at low temperatures, there is considerable uncertainty in the rheology of quartz and feldspar approaching the brittle-plastic transition (Hirth and Kohlstedt, 2015; Paterson, 1987). The goal of the present study is to investigate the rheology of quartz and feldspar at this critical range of high strain-rate, low temperature conditions using nanoindentation.

Nanoindentation is a common technique in materials science and has gained attention in the geosciences as a means to study plastic deformation of geologic materials at low temperatures ($T < 0.3T_m$, where T_m is the melting temperature of the material). The geometry of the

* Corresponding author.
E-mail address: msly@wustl.edu (M.K. Sly).

https://doi.org/10.1016/j.tecto.2023.229850
Received 22 April 2022; Received in revised form 1 March 2023; Accepted 5 April 2023
Available online 20 April 2023

nanoindenter tip produces self-confined deformation that inhibits brittle mechanisms and produces elastoplastic deformation at conditions not easily achieved by conventional rock deformation experiments (Tabor, 1970). Quartz has previously been studied using nanoindentation at room temperature (Ceccato et al., 2022; Goldsby et al., 2004) and at elevated temperatures (Strozewski et al., 2021). Feldspar has received less attention but was included in room temperature nanoindentation studies by Broz et al. (2006) and Whitney et al. (2007).

In this study we investigate the rheology of orthoclase feldspar, plagioclase feldspar (An0–15, e.g. Rutter and Neumann, 1995), and quartz from a single granitic specimen at temperatures and strain-rates relevant to the brittle to semi-brittle mid to upper crust. We focus on temperatures of $T = 23$–500 °C, which is comparable to the conditions where microcracks and faults are abundant ($T \lesssim 400$ °C, e.g., Scholz, 1988; Sibson, 1986) and at strain-rates of $\dot{\varepsilon} \sim 10^{-4}$–$10^{-1}$ s^{-1}, which is comparable to the rate of deformation during aseismic slow slip events (e.g., Rowe et al., 2011).

2. Methods

2.1. Specimen preparation and initial characterization

Nanoindentation experiments were conducted within individual grains of quartz, plagioclase, and orthoclase feldspar from a specimen of granite (likely from the Narragansett Pier plutonic group), which was collected at a road cut of State Highway 3 near Westerly, Rhode Island. 10x10x1 mm samples were cut from a larger block and polished using progressively finer diamond grit, with a final polish using 0.02 μm colloidal silica. Phase, grain-size, and crystallographic orientation of individual grains were determined using an Oxford Instruments Electron Backscatter Diffraction (EBSD) system on a JEOL 7001 FLV scanning electron microscope (SEM), operating at an accelerating voltage of 20 kV and working distance of 19 mm. The water content of the individual minerals in the specimen was not measured as recent studies have demonstrated that water concentration has no effect on the indentation hardness in of quartz (Ceccato et al., 2022; Strozewski et al., 2021).

In this study, grain orientation refers to the crystallographic direction parallel to the direction of indentation, which is appropriate because the indentation method produces nearly isotropic deformation around the axis of the indentation. Grains were selected to cover a range of crystallographic orientations in order to determine any anisotropy in indentation hardness. Five crystallographic orientations were chosen for each quartz and plagioclase and four crystallographic orientations were chosen for orthoclase. Indentation of these minerals was normal to the following planes: (0001), $\{11\bar{2}0\}$, $\{10\bar{1}0\}$, $\{11\bar{2}1\}$, and $\{10\bar{1}1\}$ for quartz; (100), (010), (001), (011), and (111) for plagioclase; (100), (001), (011), and (102) for orthoclase. Because the tested grains are in a natural sample, it is difficult to find grains with the exact crystallographic orientation desired, and so we consider the range of acceptable orientations to be within 10° of the target orientations. Fig. 1 shows a section of one EBSD map highlighting some of the grains selected for mechanical testing by nanoindentation.

2.2. Nanoindentation

We performed load-controlled nanoindentation experiments using a diamond Berkovich indenter probe in a Hysitron TI 950 Triboindenter equipped with an xSol 800 heated stage capable of achieving temperatures of up to 800 °C. The stage heats the sample using two heaters one above and one below, and the tip is heated by being near the heaters. Individual indentations consist of an eight second loading segment to a maximum load of 8 mN followed by a two second hold at the maximum load then eight seconds of unloading. The maximum load of 8 mN was chosen to ensure that the indents are sufficiently deep to avoid effects of misshapen or blunted indenter tips. We note that indentation size may affect the mechanical response (e.g., Kumamoto et al., 2017), however using a constant maximum load means that systematic differences in indentation hardness are only a function of material properties.

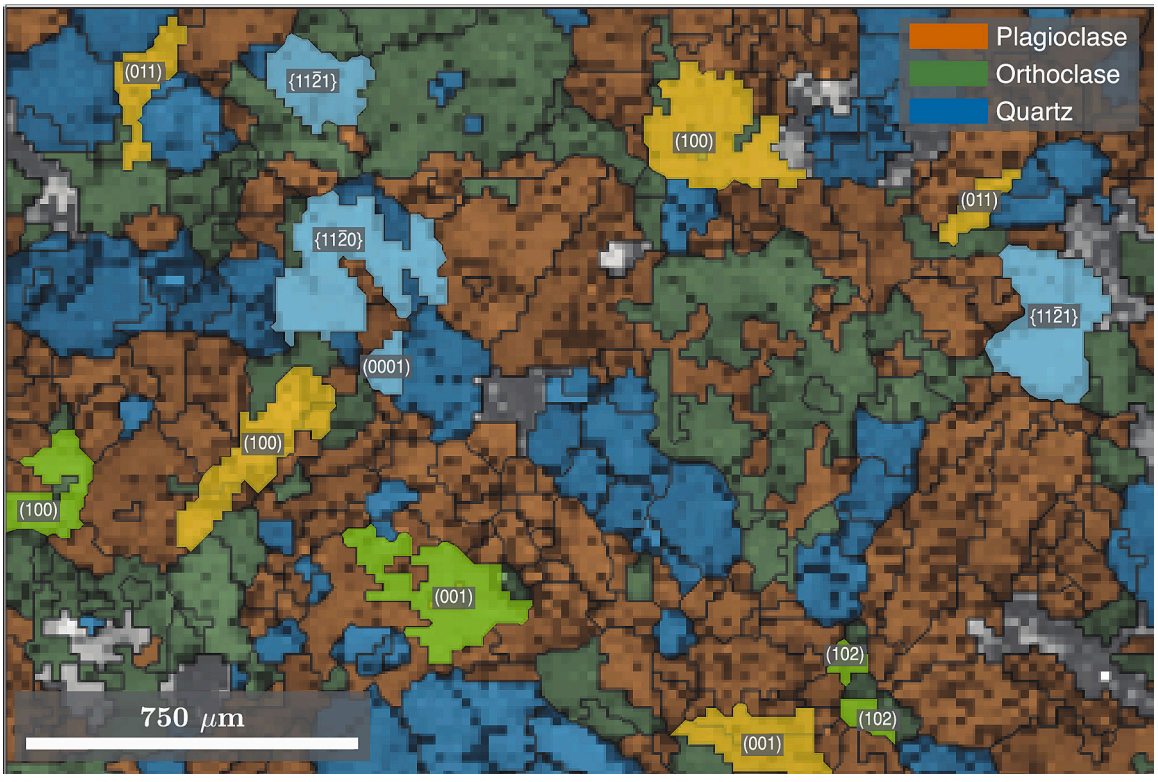

Fig. 1. A section of the electron backscatter diffraction (EBSD) map of one tested sample overlaid on the band contrast image. Grains selected for testing are highlighted with the orientation indicated.

Additionally, previous work has studied the effects of indentation size in quartz across the range of loads achievable by our experimental apparatus and procedures and found little correlation between indent size and hardness (Strozewski et al., 2021).

During each indent, the load, P, and displacement, h, were recorded simultaneously. Load measurements have a nominal resolution of <1 nN and displacement measurements have a nominal resolution of <0.02 nm. From the load and displacement measurements, the indentation hardness, H, and a reduced elastic modulus, E_r, were determined. The reduced elastic modulus is related to the Young's modulus using the following equation (Fischer-Cripps, 2011):

$$\frac{1}{E_r} = \left(\frac{1-\nu^2}{E}\right)_{sample} + \left(\frac{1-\nu^2}{E}\right)_{indenter} \quad (1)$$

where E is Young's modulus and ν is Poisson's ratio, and the subscripts refer to the properties of the sample and the indenter tip. The Young's modulus and Poisson's ratio for the indenter tip are 1140 GPa and 0.07, respectively.

We used the shape of the load-displacement curve to assess the quality of the data (e.g., Sly et al., 2020). Indents with atypical load-displacement curves (e.g., large displacement at low loads, or kinks in the loading or unloading curves) may have been performed on something other than the flat, polished sample surface and been affected by surface roughness, defects, or debris. Additionally, these load-displacement curves could indicate that the tip was not thermally equilibrated with the sample during experiments above room temperature. As a result, indents with atypical load-displacement curves are excluded from the following calculations.

Multiple indents were made in each selected grain at temperatures of 23, 100, 200, 300, 400, and 500 °C. The maximum temperature was chosen to avoid the $\alpha - \beta$ quartz transition at 573 °C. Quartz heated through this transition may fracture due to the volume change, destroying the specimens (Strozewski et al., 2021).

2.3. Yield stress and flow law parameters

Indentation hardness (H) is related to yield stress (σ_y) by a constraint factor, C (Fischer-Cripps, 2011; Tabor, 1970):

$$H = C\sigma_y \quad (2)$$

C falls between the elastic limit, 1.1, and the plastic limit, 3, depending on the ratio of Young's modulus to yield stress for a given material (Johnson, 1970). Materials with high ratios ($E/\sigma_y > 133$) typically have constraint factors around 3, and materials with lower E/σ_y ratios can have constraint factors closer to the elastic limit (Fischer-Cripps, 2011; Shaw and DeSalvo, 2012). In this work we used models from four different studies to determine the values of the constraint factor and the yield stress from indentation hardness and modulus (1. Johnson, 1970; 2. Evans and Goetze, 1979; 3. Mata et al., 2002 and Mata and Alcalá, 2003; 4. Ginder et al., 2018). Johnson (1970) models an expanding cavity in an elastic-plastic body to determine the relationship between indentation hardness and yield stress. Evans and Goetze (1979) use the model from Johnson (1970) and experimental results to develop an empirical model. Mata and Alcalá (2003) use finite element analysis of indentation in metals to develop a similar theoretical model. Ginder et al. (2018) take a similar approach to that of Johnson (1970) except using an expanding cavity in a power law creeping body rather than an elastic-plastic body. Each of these models is based on different assumptions, however at the present time there is no compelling empirical or theoretical basis for selecting one over the others. Hence results using each study's model are reported in this work (see Sly et al. (2020) for further discussion). Yield stresses calculated using these models were then used to determine the parameters for a constitutive flow law for low temperature plasticity limited by lattice resistance to dislocation motion

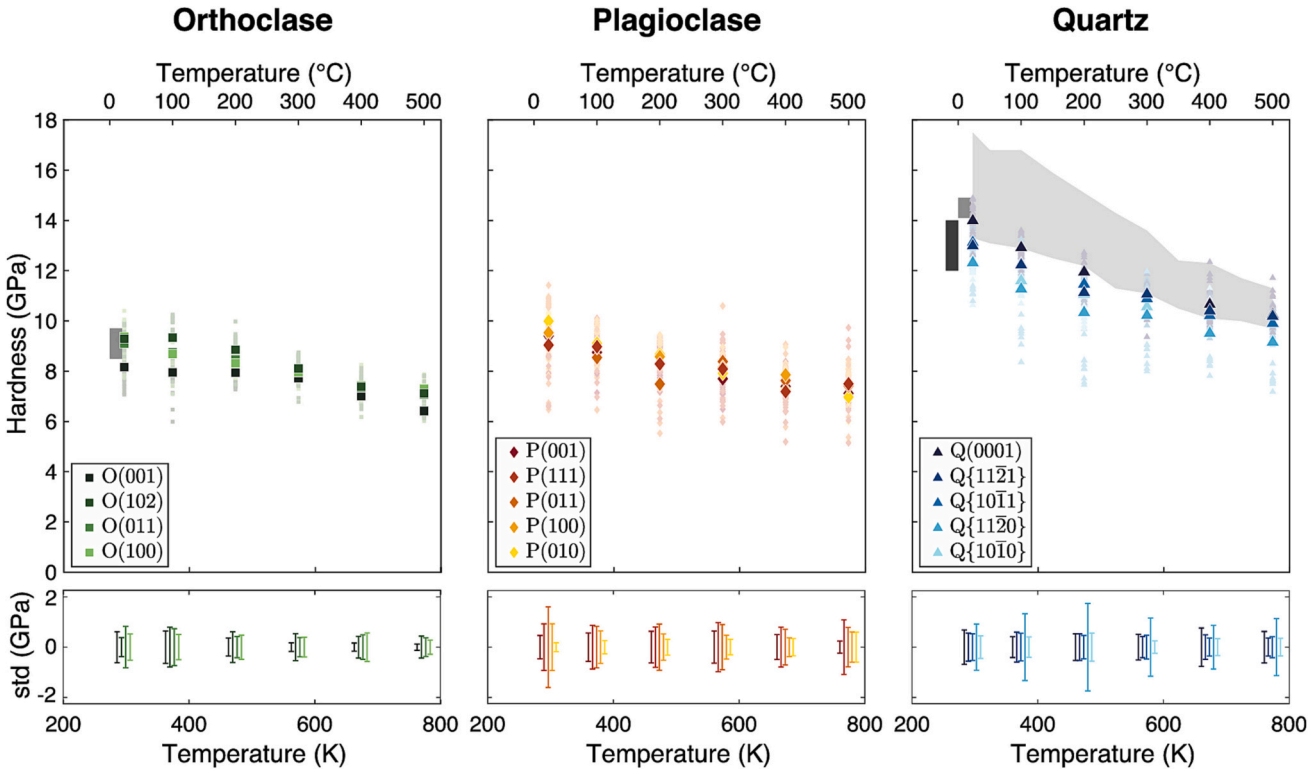

Fig. 2. Indentation hardness plotted against temperature for the three phases: orthoclase, plagioclase, and quartz. The colors represent orientation, and each error bar represents ±1 standard deviation for a given orientation. The results from previous nanoindentation studies are shown as gray regions (dark gray, Goldsby et al., 2004; medium gray, Broz et al., 2006 and Whitney et al., 2007; and light gray, Strozewski et al., 2021). The studies of Goldsby et al. (2004), Broz et al. (2006), and Whitney et al. (2007) were all conducted at room temperature and are offset here for clarity.

(see eq. 2.12 of Frost and Ashby, 1982):

$$\dot{\varepsilon} = A\sigma^2 exp\left\{ -\frac{H^*}{RT}\left[1 - \left(\frac{\sigma}{\sigma_p}\right)^p\right]^q \right\} \quad (3)$$

Here $\dot{\varepsilon}$ is strain rate, σ is stress, σ_p is athermal Peierls stress (the stress required to move a dislocation at 0 K, henceforth referred to simply as the "Peierls stress"), H^* is activation enthalpy, T is temperature, R is the gas constant, and A, p, and q are material parameters. p and q are unitless quantities with values ranging from 0.5 to 1 and 1 to 2, respectively, and depend on the energy barriers to dislocation motion (Kocks et al., 1975). The strain rates for our experiments are determined using the last 20 nm of loading, where we assume the experiment has reached a quasi-steady state (e.g., Kranjc et al., 2016; Thom et al., 2022).

We used a grid search technique to determine the unknown flow law parameters. The exponential material parameters, p and q, were fixed at four selected combinations ((p,q) = (1,1), (1,2), (0.5,1), (0.5,2), which represent the extremes of the range for each parameter) and a grid of values for the activation enthalpy, H^*, Peierls stress, σ_p, and prefactor, A, were chosen to cover a range of possible values for each. In the grids, activation enthalpy ranged from 100 to 1000 kJ/mol in 100 kJ/mol steps; Peierls stress ranged from 3 to 25 GPa in 1 GPa steps; the prefactor ranged from log(A) = −2 to log(A) = 12 GPa^{-2} s^{-1} in 1 log unit steps. One grid was produced for each of the four models for the yield stress and for each of the four combinations of exponents p and q, resulting in 16 3-dimensional grids. Yield stress was calculated for each point in the grid at the same temperatures tested in our study. The values of yield stress determined in the grids were compared to the respective calculations of yield stress based on the experimental measurements, and root mean square error (RMSE) was calculated using the following equation to determine the goodness of fit.

$$RMSE = \sqrt{\frac{\sum_i (y_i - \hat{y}_i)^2}{N}} \quad (4)$$

where y_i are the yield stress values from the experimental results, $\hat{y}_i$ are the values determined by the grid search at the relevant temperature, and N is the total number of indents. The parameter combinations with the lowest 1% RMSE values are deemed acceptable and selected as possible solutions for each grid (Supplemental Tables 5–8).

3. Results

The indentation hardness of orthoclase, plagioclase, and quartz all decrease with increasing temperature (Fig. 2 and Table 1). At 23 °C, quartz has the greatest indentation hardness of the three phases with an average hardness of 12.89 ± 0.87 GPa (all uncertainties are 1σ, based on repeat measurements). Plagioclase and orthoclase are weaker with H values of 9.49 ± 0.93 and 8.96 ± 0.77 GPa, respectively. In general, this trend continues with increasing temperature. At 500 °C, the indentation hardnesses of quartz, plagioclase, and orthoclase are 9.87 ± 0.73, 7.29 ± 0.69, and 6.97 ± 0.47 GPa, respectively.

The crystallographic orientation of each phase has a moderate effect

Table 1
Indentation hardness for orthoclase, plagioclase, and quartz as a function of temperature and orientation shown as mean ± 1 standard deviation, along with the number of indents considered.

Hardness (GPa)

Temperature	Orthoclase									
(°C)	All		(001)		(102)		(011)		(100)	
23	8.96 ± 0.77	N = 93	8.17 ± 0.61	N = 26	9.29 ± 0.38	N = 24	9.10 ± 0.83	N = 18	9.37 ± 0.52	N = 25
100	8.65 ± 0.83	N = 91	7.95 ± 0.64	N = 26	9.34 ± 0.79	N = 22	8.75 ± 0.73	N = 18	8.69 ± 0.50	N = 25
200	8.37 ± 0.58	N = 94	7.94 ± 0.36	N = 27	8.86 ± 0.61	N = 23	8.47 ± 0.42	N = 18	8.32 ± 0.48	N = 26
300	7.95 ± 0.41	N = 92	7.72 ± 0.17	N = 25	8.11 ± 0.54	N = 23	8.04 ± 0.38	N = 18	7.96 ± 0.39	N = 26
400	7.29 ± 0.47	N = 85	7.01 ± 0.16	N = 22	7.38 ± 0.43	N = 20	7.35 ± 0.49	N = 18	7.43 ± 0.57	N = 25
500	6.97 ± 0.47	N = 85	6.42 ± 0.13	N = 23	7.12 ± 0.44	N = 22	7.07 ± 0.37	N = 18	7.31 ± 0.28	N = 22

Temperature	Plagioclase											
(°C)	All		(001)		(011)		(111)		(100)		(010)	
23	9.49 ± 0.93	N = 118	9.40 ± 0.46	N = 25	9.51 ± 1.60	N = 17	9.04 ± 0.93	N = 25	9.53 ± 0.92	N = 26	9.99 ± 0.17	N = 25
100	8.90 ± 0.65	N = 108	8.75 ± 0.56	N = 25	8.54 ± 0.83	N = 13	8.97 ± 0.87	N = 19	8.95 ± 0.64	N = 25	9.11 ± 0.26	N = 26
200	8.33 ± 0.73	N = 120	8.30 ± 0.63	N = 28	7.49 ± 0.92	N = 17	8.29 ± 0.80	N = 22	8.58 ± 0.52	N = 27	8.68 ± 0.31	N = 26
300	8.02 ± 0.69	N = 114	7.70 ± 0.64	N = 25	8.38 ± 0.90	N = 14	8.09 ± 0.98	N = 23	8.15 ± 0.47	N = 27	7.92 ± 0.31	N = 25
400	7.46 ± 0.60	N = 121	7.39 ± 0.50	N = 27	7.63 ± 0.71	N = 18	7.19 ± 0.79	N = 23	7.86 ± 0.37	N = 27	7.25 ± 0.34	N = 26
500	7.29 ± 0.69	N = 116	7.12 ± 0.24	N = 30	7.42 ± 0.78	N = 17	7.50 ± 1.09	N = 19	7.50 ± 0.60	N = 28	6.97 ± 0.59	N = 22

Temperature	Quartz											
(°C)	All		(0001)		{1121}		{1011}		{1120}		{1010}	
23	12.89 ± 0.87	N = 136	14.00 ± 0.69	N = 23	12.99 ± 0.56	N = 27	13.13 ± 0.53	N = 24	12.32 ± 0.92	N = 26	12.35 ± 0.45	N = 36
100	12.01 ± 0.91	N = 138	12.92 ± 0.41	N = 24	12.23 ± 0.60	N = 26	12.26 ± 0.55	N = 26	11.28 ± 1.33	N = 26	11.61 ± 0.41	N = 36
200	11.15 ± 1.02	N = 136	11.95 ± 0.53	N = 21	11.13 ± 0.53	N = 27	11.47 ± 0.46	N = 27	10.34 ± 1.74	N = 27	11.06 ± 0.56	N = 34
300	10.72 ± 0.68	N = 138	10.89 ± 0.51	N = 23	11.06 ± 0.42	N = 27	10.89 ± 0.47	N = 27	10.22 ± 1.16	N = 26	10.56 ± 0.25	N = 35
400	10.24 ± 0.70	N = 134	10.66 ± 0.76	N = 25	10.40 ± 0.49	N = 25	10.22 ± 0.36	N = 22	9.51 ± 0.87	N = 27	10.39 ± 0.34	N = 35
500	9.87 ± 0.73	N = 122	10.25 ± 0.63	N = 20	10.18 ± 0.36	N = 24	9.90 ± 0.42	N = 26	9.16 ± 1.14	N = 23	9.90 ± 0.35	N = 29

Table 2
Average yield stress values irrespective of orientation for orthoclase, plagioclase, and quartz for each of the four models (1. Johnson, 1970; 2. Evans and Goetze, 1979; 3. Mata et al., 2002 and Mata and Alcalá, 2003;4. Ginder et al., 2018) shown as mean ± 1 standard deviation.

Temperature	Johnson (1970) Yield Stress (GPa)		
(°C)	Orthoclase	Plagioclase	Quartz
23	8.15 ± 0.70	8.63 ± 0.84	11.72 ± 0.79
100	7.86 ± 0.75	8.09 ± 0.59	10.92 ± 0.82
200	7.61 ± 0.52	7.57 ± 0.67	10.14 ± 0.93
300	7.22 ± 0.37	7.29 ± 0.63	9.74 ± 0.62
400	6.63 ± 0.42	6.78 ± 0.54	9.31 ± 0.64
500	6.33 ± 0.43	6.63 ± 0.63	8.98 ± 0.66

Temperature	Evans and Goetze (1979) Yield Stress (GPa)		
(°C)	Orthoclase	Plagioclase	Quartz
23	8.14 ± 0.71	8.56 ± 0.94	11.72 ± 0.79
100	7.83 ± 0.81	7.94 ± 0.77	10.92 ± 0.82
200	7.46 ± 0.64	7.30 ± 0.89	10.10 ± 0.93
300	6.84 ± 0.60	6.73 ± 1.07	9.65 ± 0.67
400	5.92 ± 0.88	5.71 ± 1.03	9.07 ± 0.64
500	5.40 ± 1.02	5.44 ± 1.08	8.60 ± 0.88

Temperature	Mata and Alcalá (2003) Reference Stress (GPa)		
(°C)	Orthoclase	Plagioclase	Quartz
23	4.89 ± 0.58	4.96 ± 0.57	7.10 ± 0.65
100	4.50 ± 0.53	4.55 ± 0.46	6.46 ± 0.46
200	4.22 ± 0.39	4.17 ± 0.45	5.88 ± 0.35
300	3.90 ± 0.3	3.86 ± 0.45	5.44 ± 0.33
400	3.51 ± 0.36	3.44 ± 0.38	5.04 ± 0.29
500	3.25 ± 0.35	3.36 ± 0.42	4.81 ± 0.31

Temperature	Ginder et al. (2018) Yield Stress (GPa)		
(°C)	Orthoclase	Plagioclase	Quartz
23	3.65 ± 0.31	3.87 ± 0.38	5.25 ± 0.35
100	3.52 ± 0.34	3.62 ± 0.26	4.89 ± 0.37
200	3.41 ± 0.23	3.39 ± 0.30	4.54 ± 0.42
300	3.24 ± 0.17	3.27 ± 0.28	4.36 ± 0.28
400	2.97 ± 0.19	3.04 ± 0.24	4.17 ± 0.29
500	2.84 ± 0.19	2.97 ± 0.28	4.02 ± 0.30

on indentation hardness with the most prominent anisotropy seen in orthoclase and quartz. In orthoclase, grains oriented for indentation normal to the (001) plane have the lowest values for hardness (8.17 ± 0.61 GPa; approximately 91.18% of the average of all grains at 23 °C), while grains in any of the other orientations exhibit hardnesses greater than the average. In quartz, grains oriented for indentation normal to the (0001) typically have the greatest values for hardness (14.00 ± 0.69 GPa; approximately 108.61% of the average of all grains at 23 °C), and grains oriented for indentation normal to the $\{11\bar{2}0\}$ and $\{10\bar{1}0\}$ planes have the smallest values for hardness (12.32 ± 0.92 and 12.35 ± 0.45 GPa; approximately 95.58 and 95.81% of the average of all grains at 23 °C). One grain in the $\{11\bar{2}0\}$ orientation is particularly weak and lowers the average hardness reported for that orientation. However, even excluding these data, the $\{11\bar{2}0\}$ orientation is still relatively weak. In plagioclase, grains in the (001) orientation are slightly weaker than average (9.40 ± 0.46 GPa; approximately 99.05% of the average at 23 °C) and grains in the (100) orientation are consistently slightly harder than average (9.53 ± 0.92 GPa; approximately 100.42% of the average of all grains at 23 °C), though all of the tested orientations in plagioclase have equivalent hardnesses within error at a given temperature.

The same trends are observed in the calculated yield stresses, with quartz systematically stronger than both feldspars, though there are some differences depending on which model is used to determine yield stress (Table 2 and Supplementary Table 1–4). The anisotropy observed in the indentation hardness of each phase is also present in the yield stress. The models from Johnson (1970) (orthoclase: $\sigma_y = 8.15 \pm 0.70$ GPa; plagioclase: $\sigma_y = 8.63 \pm 0.84$ GPa; quartz: $\sigma_y = 11.72 \pm 0.79$ GPa at 23 °C) and Evans and Goetze (1979) (orthoclase: $\sigma_y = 8.09 \pm 0.74$ GPa; plagioclase: $\sigma_y = 8.56 \pm 0.94$ GPa; quartz: $\sigma_y = 11.72 \pm 0.79$ GPa at 23 °C) both result in constraint factors at or near the elastic limit of $C = 1.1$, which means that the yield stress values determined by each model are quite similar. The difference between these two models is observed at higher temperatures when the constraint factors determined from the Evans and Goetze (1979) model begin to increase, which results in lower yield stresses (orthoclase: $\sigma_y = 5.20 \pm 1.06$ GPa; plagioclase: $\sigma_y = 5.44 \pm 1.04$ GPa; quartz: $\sigma_y = 8.77 \pm 0.76$ GPa at 500 °C) than those determined using the Ginder et al. (2018) model (orthoclase: $\sigma_y = 6.33 \pm 0.43$ GPa; plagioclase: $\sigma_y = 6.63 \pm 0.63$ GPa; quartz: $\sigma_y = 8.98 \pm 0.66$ GPa at 500 °C). The yield stresses determined using the Mata and Alcalá (2003) (orthoclase: $\sigma_y = 4.69 \pm 0.52$ GPa; plagioclase: $\sigma_y = 4.96 \pm 0.57$ GPa; quartz: $\sigma_y = 7.45 \pm 0.76$ GPa at 23 °C) and Ginder et al. (2018) (orthoclase: $\sigma_y = 6.65 \pm 0.31$ GPa; plagioclase: $\sigma_y = 3.87 \pm 0.38$ GPa; quartz: $\sigma_y = 5.25 \pm 0.35$ GPa at 23 °C) models are systematically lower, which is reflected in the higher constraint factors; $C = 1.74 \pm 0.13$–2.00 ± 0.12 for the Mata and Alcalá (2003) model, and $C = 2.46$ for the Ginder et al. (2018) model.

The yield stress calculated from each of these four models are used to determine flow law parameters, A, H^*, and σ_p using a grid search approach described in the Methods above. The grid search results show that, for each of the three phases, the Peierls stress, σ_p, is generally well-constrained within a range of ±2 GPa. Some grids with $q = 2$ exhibit larger Peierls stresses, as there is generally more curvature in the flow laws at low temperatures (T ⟨200K). The prefactor, A, and activation enthalpy, H^*, are less well constrained and covary with one another often resulting in acceptable values covering the range of the whole grid (Fig. 3).

Rather than present a single flow law for each phase, here we show a range of plausible flow laws (Fig. 4 and Supplementary Figs. 1–15). The regions shown here are composed of several combinations of flow law parameters, each with an RMSE less than or equal to one standard deviation for yield stress of a given phase and model. Fig. 4 is an example of the flow laws calculated for the parameters $p = 1$ and $q = 1$ with yield stress determined using the Evans and Goetze (1979) model (the flow laws for the other three yield stress models can be found in the supplemental material). For all combinations of model and p and q pairs, quartz is stronger than both plagioclase and orthoclase feldspars at low temperatures with athermal Peierls stresses three to four GPa higher for each model and combination of p and q.

At higher temperatures (T > ~700 °C), some of the model combinations show convergence of the rheology of the phases, suggesting that increasing temperature may have a greater effect on the strength of quartz than that of feldspar. Additional indents in select grains of quartz, plagioclase, and orthoclase were performed at temperatures above the $\alpha - \beta$ quartz transition (573 °C) and the indentation hardness and yield stress of quartz remain higher than both feldspars as temperature increases. However, the quartz grains in the specimen began to show signs of fracture caused by heating and cooling through the $\alpha - \beta$ transition. Because of this, we could not perform more indents and the results from the indents we do have may not accurately represent the plastic deformation of the materials.

4. Discussion

4.1. Comparisons to previous indentation studies

Orthoclase feldspar and quartz have previously been studied using nanoindentation. Studies on orthoclase feldspar indented normal to the

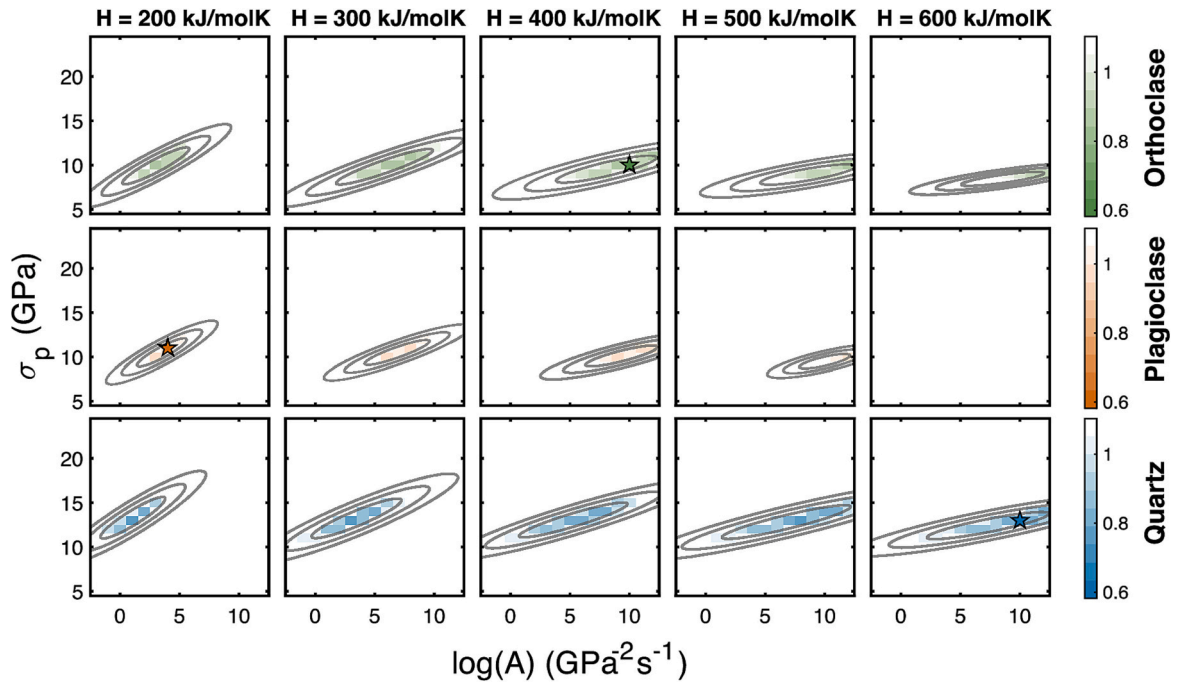

Fig. 3. A subset of the grid search results for each of the three phases for yield stress determined using the model of Evans and Goetze (1979) with $p = 1$ and $q = 1$. The colored boxes in the grid represent combinations of the three varying parameters: activation enthalpy (H^*), pre-factor (A), and Peierls stress (σ_p), that result in root mean square errors (RMSE) less than twice the standard deviation of the maximum experimental results. The color represents the goodness of fit via RMSE. The three ellipses represent the 2-dimensional 99.7%, 95%, and 68% confidence intervals. The parameter combination with the lowest RMSE for each phase is marked with a colored star.

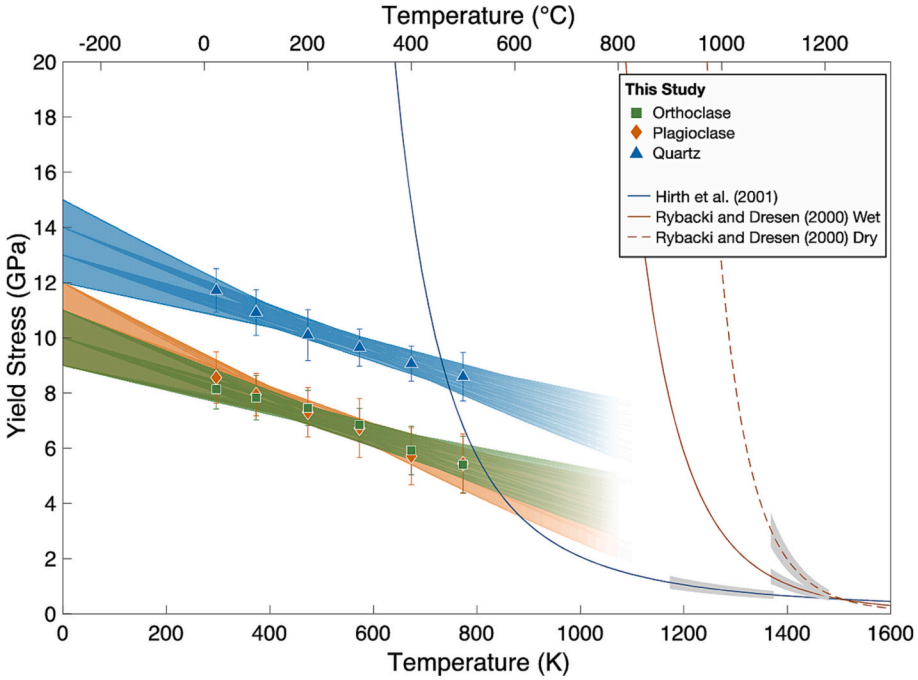

Fig. 4. The parameter combinations that yield the lowest 1% of RMSE values for each model and each p and q are used to calculate flow laws for yield stress as a function of temperature. The flow laws for each phase are combined into a region of possible values. Examples of these flow law regions produced from the grid search results for yield stress determined using the model of Evans and Goetze (1979) and $p = 1$ and $q = 1$ are shown here. For comparison, flow laws from previous studies (quartz: Hirth et al., 2001; plagioclase: Rybacki and Dresen, 2000) are shown. The shaded regions around these flow laws show the range of experimental data used to produce the flow law. The flow law from Hirth et al. (2001) was determined using data from both experimental and natural deformation.

(101) plane (Broz et al., 2006; Whitney et al., 2007) report room temperature indentation hardness of ~9.1 GPa, which is in good agreement with the indentation hardness determined in our studies. Natural and synthetic quartz samples have been indented normal to a $\{10\bar{1}0\}$ plane (Goldsby et al., 2004; Strozewski et al., 2021) and normal to the (1000) plane (Broz et al., 2006; Strozewski et al., 2021; Whitney et al., 2007). The results presented in this study for the relevant orientations at room temperature are also in good agreement with the room temperature hardness determined for natural quartz specimens in Goldsby et al. (2004) (~12–14 GPa), Broz et al. (2006) (14.54 ± 0.42 GPa), and Whitney et al. (2007) (14.5 ± 0.4 GPa), and are just below the lower range reported in Strozewski et al. (2021) over a range of elevated temperatures (15.35 ± 1.40–17.47 ± 2.30 GPa) (Fig. 2). One possible explanation for the modest discrepancy among these results is the role of

pre-existing defects. Recently, Wallis et al. (2020) performed nanoindentation on olivine using a spherical indenter and report a slightly lower yield stress and less ordered dislocations in a specimen with preexisting dislocations compared to a specimen that was nominally dislocation-free. Similarly, a study by Ceccato et al. (2022) on the indentation of quartz report that the initial density of defects in the sample may play a significant role on the strength. These studies suggest that the differences in indentation hardness could be explained in this way if the lab-grown single crystals studied by Strozewski et al. (2021) have a lower initial dislocation density than that of a typical plutonic quartz specimen ($\sim 10^{12}$ m^{-2}; Stesky, 1978).

Feldspar and quartz have also been studied using microindentation techniques. The studies by Broz et al. (2006) and Whitney et al. (2007) both report a microhardness of ~6.9 GPa for orthoclase. Huang et al. (1985) studied orthoclase and laboradorite with Vickers hardnesses of ~9 GPa for both phases at 20 °C and ~ 7.5–8.5 GPa at 550–650 °C. Evans (1984) studied quartz with indentation hardnesses ranging from ~10 GPa at 250 °C to ~7 GPa at 820 °C. These values are slightly lower than the results from our study. This difference could be attributed to the indentation size effect or differences in deformation mechanisms, since Vickers hardness testing often results in cracking of brittle materials (See, for example, Fig. 4 in Huang et al., 1985).

4.2. Relevance to crack propagation and faulting

The results from our nanoindentation experiments show quartz as the stronger phase over a wide range of temperatures, which is contrary to what has been observed in the majority of shear zones and experiments (e.g., Fossen and Cavalcante, 2017; Tullis and Yund, 1992) although other studies have made similar observations (Ji et al., 2004, 2000). Typically, the brittle-ductile transition in quartzofeldspathic rocks is described as brittle fracture in feldspar (primarily along cleavage planes) and viscoplasticity in quartz (e.g., dislocation creep or dissolution precipitation creep), suggesting that feldspar is stronger than quartz (e.g., Tullis, 2002). The nanoindentation experiments in this study inhibit brittle deformation at low temperatures by design, and therefore allow us to induce different deformation mechanisms than those commonly observed in higher temperature shear zones.

The plastic rheology of feldspar and quartz determined by nanoindentation complement data from experiments conducted at higher temperature and pressure, and may be used to improve modeling of faults, cracks, and semi-brittle deformation in the mid to upper continental crust. It has been theorized and observed that macroscopic shear faults form through the formation, propagations, and coalescence of grain-scale microcracks (Cox and Scholz, 1988; Lockner et al., 1991; Nemat-Nasser and Horii, 1982). Stresses at crack tips can be much higher than the background stresses in the region, and a plastic zone often exists in the immediate vicinity of crack tips where stresses can exceed the plastic limit (Griffith, 1920; Rice, 1968; Rice and Rosengren, 1968). Additionally, at a larger scale, modeling by Dunham et al. (2011a, 2011b) shows that regions of plastic deformation around faults are necessary to eliminate fault opening.

We suggest that the results of the present study may be especially relevant to high stress regions near the brittle-ductile transition, where microcracks and faults are abundant. These results are especially useful in the vicinity of cracks with sufficiently small radii of curvature or sufficiently large aspect ratios. The maximum stress concentration factor around elliptical defects in a pure shear stress state can be determined using the following equation (Pilkey et al., 2020, p. 220).

$$K_T = \frac{(a+b)^2}{ab} \tag{5}$$

where K_T is the stress concentration factor, a is the length of the semi-major axis, and b is the length of the semiminor axis. The World Stress Map (Heidbach et al., 2018, 2016) has observed stresses in the Earth's crust to be on the order of 10 MPa with a mean value of ~13 MPa from a variety of measurement techniques. A study by Sprunt and Brace (1974) report the aspect ratios (a/b) of some cavities in Westerly granite are on the order of 10^3 and the longest cavities with low aspect ratios are on the order of 100 μm long. If we assume an elliptical crack with an aspect ratio of 10^3, a semi major axis of ~100 μm, and background stress of ~10 MPa, the stresses concentrated at the tips of the crack will be ~10 GPa. Thus, approximate stresses at crack tips in nature are comparable to the yield stresses determined in this study. Hence, we conclude that low-temperature plastic rheologies, such as those determined here, may be well-suited for modeling deformation near crack tips and in semi-brittle deformation regimes.

5. Conclusions

We have performed nanoindentation experiments on oriented grains of quartz and two feldspars in a medium-grained granite. Our results show that quartz has the highest indentation hardness of the three (12.89 GPa at 23 °C and 9.87 GPa at 500 °C), and the two feldspars have comparable hardnesses (orthoclase: 8.96 GPa at 23 °C and 6.97 GPa at 500 °C; plagioclase: 9.49 GPa at 23 °C and 7.29 GPa at 500 °C). These trends continue when indentation hardness is converted to yield stress using four different models (1. Johnson, 1970; 2. Evans and Goetze, 1979; 3. Mata et al., 2002 and Mata and Alcalá, 2003; 4. Ginder et al., 2018). Multiple flow laws for low temperature plasticity limited by lattice resistance have been determined for the calculated yield stresses using a grid search technique. The results determined here show feldspars have a lower yield stress than quartz, which agrees with the results from prior nanoindentation studies. The conditions of our experiments resemble the conditions around the tips of cracks in the mid to upper crust, and therefore the results should be applied in geologic settings where brittle and semi-brittle deformation processes dominate.

CRediT authorship contribution statement

Michael K. Sly: Methodology, Software, Formal analysis, Investigation, Data curation, Visualization, Writing – original draft. **Katharine Padilla:** Investigation, Writing – review & editing. **Katharine M. Flores:** Conceptualization, Funding acquisition, Supervision, Writing – review & editing. **Philip Skemer:** Conceptualization, Funding acquisition, Supervision, Writing – review & editing.

Declaration of Competing Interest

The authors declare that they have no known competing financial interests or personal relationships that could have appeared to influence the work reported in this paper.

Data availability

Data will be made available on request.

Acknowledgements

This work is funded by NSF EAR-1726165 to Skemer and Flores. Additional instrument support is provided by the Institute of Materials Science and Engineering at Washington University in St. Louis.

Appendix A. Supplementary data

Supplementary data to this article can be found online at https://doi.org/10.1016/j.tecto.2023.229850.

References

Broz, M.E., Cook, R.F., Whitney, D.L., 2006. Microhardness, toughness, and modulus of Mohs scale minerals. Am. Mineral. 91, 135–142. https://doi.org/10.2138/am.2006.1844.

Bürgmann, R., Dresen, G., 2008. Rheology of the lower crust and upper mantle: evidence from rock mechanics, geodesy, and field observations. Annu. Rev. Earth Planet. Sci. 36, 531–567. https://doi.org/10.1146/annurev.earth.36.031207.124326.

Ceccato, A., Menegon, L., Hansen, L., 2022. Strength of Dry and Wet Quartz in the Low-Temperature Plasticity Regime: Insights from Nanoindentation, p. 49. https://doi.org/10.1029/2021GL094633.

Cox, S.J.D., Scholz, C.H., 1988. On the formation and growth of faults: an experimental study. J. Struct. Geol. 10, 413–430. https://doi.org/10.1016/0191-8141(88)90019-3.

Dunham, E.M., Belanger, D., Cong, L., Kozdon, J.E., 2011a. Earthquake ruptures with strongly rate-weakening friction and off-fault plasticity, part 1: Planar faults. Bull. Seismol. Soc. Am. 101, 2296–2307. https://doi.org/10.1785/0120100075.

Dunham, E.M., Belanger, D., Cong, L., Kozdon, J.E., 2011b. Earthquake ruptures with strongly rate-weakening friction and off-fault plasticity, part 2: Nonplanar faults. Bull. Seismol. Soc. Am. 101, 2308–2322. https://doi.org/10.1785/0120100076.

Evans, B., 1984. The effect of Temperature and Impurity Content on Indentation Hardness of Quartz. J. Geophys. Res. 89, 4213–4222.

Evans, B., Goetze, C., 1979. The temperature variation of hardness of olivine and its implication for polycrystalline yield stress. J. Geophys. Res. 84, 5505. https://doi.org/10.1029/JB084iB10p05505.

Fischer-Cripps, A.C., 2011. Nanoindentation, 3rd ed. Springer, New York, NY.

Fossen, H., Cavalcante, G.C.G., 2017. Shear zones – a review. Earth Sci. Rev. 171, 434–455. https://doi.org/10.1016/j.earscirev.2017.05.002.

Frost, H.J., Ashby, F., 1982. Deformation-Mechanism Maps: The Plasticity and Creep of Metals and Ceramics. Pergamon Press.

Ginder, R.S., Nix, W.D., Pharr, G.M., 2018. A simple model for indentation creep. J. Mech. Phys. Solids 112, 552–562. https://doi.org/10.1016/j.jmps.2018.01.001.

Gleason, G.C., Tullis, J., 1995. A flow law for dislocation creep of quartz aggregates determined with the molten salt cell. Tectonophysics 247, 1–23. https://doi.org/10.1016/0040-1951(95)00011-B.

Goldsby, D.L., Rar, A., Pharr, G.M., Tullis, T.E., 2004. Nanoindentation creep of quartz, with implications for rate- and state-variable friction laws relavent to earthquake mechanics. J. Mater. Res. 19, 357–365. https://doi.org/10.1016/0040-1951(83)90266-4.

Griffith, A.A., 1920. The Phenomena O f Rupture and Flow in Solids C, pp. 163–198.

Heidbach, O., Rajabi, M., Reiter, K., Ziegler, M.O., 2016. W.T., 2016. World Stress Map Database Release 2016. V. 1.1. GFZ Data Services.

Heidbach, O., Rajabi, M., Cui, X., Fuchs, K., Müller, B., Reinecker, J., Reiter, K., Tingay, M., Wenzel, F., Xie, F., Ziegler, M.O., Zoback, Mary Lou, Zoback, Mark, 2018. The World stress Map database release 2016: Crustal stress pattern across scales. Tectonophysics 744, 484–498. https://doi.org/10.1016/j.tecto.2018.07.007.

Hirth, G., Kohlstedt, D.L., 2015. The stress dependence of olivine creep rate: Implications for extrapolation of lab data and interpretation of recrystallized grain size. Earth Planet. Sci. Lett. 418, 20–26. https://doi.org/10.1016/j.epsl.2015.02.013.

Hirth, G., Teyssier, C., Dunlap, W.J., 2001. An evaluation of quartzite flow laws based on comparisons between experimentally and naturally deformed rocks. International Journal of Earth Sciences 90 (1), 77–87. https://doi.org/10.1007/s005310000152.

Hirth, G., Tullis, J., 1992. Dislocation creep regimes in quartz aggregates. J. Struct. Geol. 14, 145–159. https://doi.org/10.1016/0191-8141(92)90053-Y.

Holyoke III, C.W., Tullis, J., 2006. Formation and maintenance of shear zones. Geology 34, 105–108. https://doi.org/10.1130/G22116.1.

Huang, Z.H., Gandais, M., Gaboriaud, R.J., 1985. Microhardness of feldspar single crystals (Or98 and An58) as a function of temperature. Bull. Mineral. 108, 835–841. https://doi.org/10.3406/bulmi.1985.7902.

Ji, S., Wirth, R., Rybacki, E., Jiang, Z., 2000. High-temperature plastic deformation of quartz-plagioclase multilayers by layer-normal compression. J. Geophys. Res. Solid Earth 105, 16651–16664. https://doi.org/10.1029/2000jb900130.

Ji, S., Jiang, Z., Rybacki, E., Wirth, R., Prior, D., Xia, B., 2004. Strain softening and microstructural evolution of anorthite aggregates and quartz–anorthite layered composites deformed in torsion. Earth Planet. Sci. Lett. 222, 377–390. https://doi.org/10.1016/j.epsl.2004.03.021.

Johnson, K.L., 1970. The correlation of indentation experiments. J. Mech. Phys. Solids 18, 115–126. https://doi.org/10.1016/0022-5096(70)90029-3.

Kocks, U.F., Argon, A.S., Ashby, M.F., 1975. Thermodynamics and Kinetics of Slip. Prog. Mater. Sci. https://doi.org/10.1016/0079-6425(75)90009-2.

Kohlstedt, D.L., Evans, B., Mackwell, S.J., 1995. Strength of the lithosphere: Constrains imposed by laboratory experiments. Journal 100, 17587–17602. https://doi.org/10.1007/978-90-481-2642-2_689.

Kranjc, K., Rouse, Z., Flores, K.M., Skemer, P., 2016. Low-temperature plastic rheology of olivine determined by nanoindentation. Geophys. Res. Lett. 42 https://doi.org/10.1002/2015GL065837.Received.

Kumamoto, K.M., Thom, C.A., Wallis, D., Hansen, L.N., Armstrong, D.E.J., Warren, J.M., Goldsby, D.L., Wilkinson, A.J., 2017. Size effects resolve discrepancies in 40 years of work on low-temperature plasticity in olivine. Sci. Adv. 1–7.

Lockner, D.A., Byerlee, J.D., Kuksenkot, V., Ponomarev, A., Sidorin, A., 1991. Quasi-static fault growth and shear fracture energy in granite. Nature 350, 39–42.

Mata, M., Alcalá, J., 2003. Mechanical property evaluation through sharp indentations in elastoplastic and fully plastic contact regimes. J. Mater. Res. 18, 1705–1709. https://doi.org/10.1557/JMR.2003.0234.

Mata, M., Anglada, M., Alcala, J., Alcalá, J., 2002. Contact deformation regimes around sharp indentations and the concept of the characteristic strain. J. Mater. Res. 17, 964–976. https://doi.org/10.1557/JMR.2002.0144.

Nemat-Nasser, S., Horii, H., 1982. Compression-induced nonplanar crack extension with application to splitting, exfoliation, and rockburst. J. Geophys. Res. 87, 6805–6821. https://doi.org/10.1029/JB087iB08p06805.

Papeschi, S., Musumeci, G., Mazzarini, F., 2018. Evolution of shear zones through the brittle-ductile transition: The Calamita Schists (Elba Island, Italy). J. Struct. Geol. 113, 100–114. https://doi.org/10.1016/j.jsg.2018.05.023.

Paterson, M.S., 1987. Problems in the extrapolation of laboratory rheological data. Tectonophysics 133, 33–43. https://doi.org/10.1016/0040-1951(87)90278-2.

Pilkey, W.D., Pilkey, D.F., Bi, Z., 2020. Peterson's Stress Concentration Factors. John Wiley & Sons.

Rice, J.R., 1968. Mathematical analysis in the mechanics of fracture. In: Fracture: An Advanced Treatise, pp. 191–310.

Rice, J.R., Rosengren, G.F., 1968. Plane strain deformation near a crack tip in a power-law hardening material. J. Mech. Phys. Solids 16, 1–12. https://doi.org/10.1016/0022-5096(68)90013-6.

Richter, B., Stünitz, H., Heilbronner, R., 2018. The brittle-to-viscous transition in polycrystalline quartz: an experimental study. J. Struct. Geol. 114, 1–21. https://doi.org/10.1016/j.jsg.2018.06.005.

Rowe, C.D., Meneghini, F., Casey Moore, J., 2011. Textural record of the seismic cycle: Strain-rate variation in an ancient subduction thrust. Geol. Soc. Spec. Publ. 359, 77–95. https://doi.org/10.1144/SP359.5.

Rutter, E.H., Neumann, D.H.K., 1995. Experimental deformation of partially molten Westerly granite under fluid-absent conditions, with implications for the extraction of granitic magmas. Journal of Geophysical Research 100 (B8). https://doi.org/10.1029/94jb03388.

Rybacki, E., Dresen, G., 2000. Dislocation and diffusion creep of synthetic anorthite aggregates. J. Geophys. Res. Solid Earth 105, 26017–26036. https://doi.org/10.1029/2000jb900223.

Rybacki, E., Dresen, G., 2004. Deformation mechanism maps for feldspar rocks. Tectonophysics 382, 173–187. https://doi.org/10.1016/j.tecto.2004.01.006.

Scholz, C.H., 1988. The brittle-plastic transition and the depth of seismic faulting. Geol. Rundsch. 77, 319–328. https://doi.org/10.1007/BF01848693.

Shaw, M.C., DeSalvo, G.J., 2012. The role of elasticity in hardness testing. Metallogr. Microstruct. Anal. 1, 310–317. https://doi.org/10.1007/s13632-012-0047-3.

Sibson, R.H., 1977. Fault rocks and fault mechanisms. J. Geol. Soc. Lond. 133 https://doi.org/10.1144/gsjgs.133.3.0191, 191 LP – 213.

Sibson, R.H., 1986. Earthquakes and rock deformation in crustal fault zones. Annu. Rev. Earth Planet. Sci. 14, 149–175. https://doi.org/10.1146/annurev.earth.14.1.149.

Sly, M.K., Thind, A.S., Mishra, R., Flores, K.M., Skemer, P., 2020. Low-temperature rheology of calcite. Geophys. J. Int. 221, 129–141. https://doi.org/10.1093/gji/ggz577.

Sprunt, E.S., Brace, W.F., 1974. Direct observation of microcavities in crystalline rocks. Int. J. Rock Mech. Min. Sci. 11, 139–150. https://doi.org/10.1016/0148-9062(74)92874-5.

Stesky, R.M., 1978. Mechanisms of high temperature frictional sliding in Westerly granite. Can. J. Earth Sci. 15, 361–375. https://doi.org/10.1139/e78-042.

Stipp, M., Stunitz, H., Heilbronner, R., Schmid, S.M., 2002a. Dynamic recrystallization of quartz: correlation between natural and experimental conditions. Geol. Soc. Lond. Spec. Publ. 200, 171–190.

Stipp, M., Stünitz, H., Heilbronner, R., Schmid, S.M., 2002b. The eastern Tonale fault zone: a "natural laboratory" for crystal plastic deformation of quartz over a temperature range from 250 to 700 °C. J. Struct. Geol. 24, 1861–1884. https://doi.org/10.1016/S0191-8141(02)00035-4.

Strozewski, B., Sly, M.K., Flores, K.M., Skemer, P., 2021. Viscoplastic Rheology of α-quartz Investigated by Nanoindentation. J. Geophys. Res. Solid Earth. https://doi.org/10.1029/2021JB022229.

Tabor, D., 1970. The hardness of solids. Rev. Phys. Technol. 1, 145.

Thom, C.A., Hansen, L.N., Breithaupt, T., Goldsby, D.L., Kumamoto, K.M., 2022. Backstresses in geologic materials quantified by nanoindentation load-drop experiments. Philos. Mag. 102, 1974–1988. https://doi.org/10.1080/14786435.2022.2100937.

Tullis, J., 2002. Deformation of granitic rocks: Experimental studies and natural examples. Rev. Mineral. Geochem. 51, 51–95. https://doi.org/10.2138/gsrmg.51.1.51.

Tullis, J., Yund, R., 1992. Chapter 4 the Brittle-Ductile transition in Feldspar Aggregates: an Experimental Study. Int. Geophys. Ser. 51, 89–117.

Wallis, D., Hansen, L.N., Kumamoto, K.M., Thom, C.A., Plümper, O., Ohl, M., Durham, W.B., Goldsby, D.L., Armstrong, D.E.J., Meyers, C.D., Goddard, R., Warren, J.M., Breithaupt, T., Drury, M.R., Wilkinson, A.J., 2020. Dislocation interactions during low-temperature plasticity of olivine and their impact on the evolution of lithospheric strength. Earth Planet. Sci. Lett. 543, 116349 https://doi.org/10.1016/j.epsl.2020.116349.

Whitney, D.L., Broz, M., Cook, R.F., 2007. Hardness, toughness, and modulus of some common metamorphic minerals. Am. Mineral. 92, 281–288. https://doi.org/10.2138/am.2007.2212.

Xiao, X., Wirth, R., Dresen, G., 2002. Diffusion creep of anorthite-quartz aggregates. J. Geophys. Res. Solid Earth 107. https://doi.org/10.1029/2001jb000789. ECV 6-1-ECV 6-15.